www.ksmrm.org JKSMRM 16(2) : 103-114, 2012
Print ISSN 1226-9751

Original Article

Improvement of a 4-Channel Spiral-Loop RF Coil Array for TMJ MR Imaging at 7T

Kyoung-Nam Kim, Young-Bo Kim, Zang-Hee Cho
Neuroscience Research Institute, Gachon University, Incheon, Republic of Korea

Purpose : In an attempt to further improve the radiofrequency (RF) magnetic (B_1) field strength in temporomandibular joint (TMJ) imaging, a 4-channel spiral-loop coil array with RF circuitry was designed and compared with a 4-channel single-loop coil array in terms of B_1 field, RF transmit (B_1^+), signal-to-noise ratio (SNR), and applicability to TMJ imaging in 7T MRI.

Materials and Methods: The single- and 4-channel spiral-loop coil arrays were constructed based on the electromagnetic (EM) simulation for the investigation of B_1 field. To evaluate the computer simulation results, the B_1 field and B_1^+ maps were measured in 7T.

Results: In the EM simulation result and MRI study at 7T, the 4-channel spiral-loop coil array found a superior B_1 performance and a higher B_1^+ profile inside the human head as well as a slightly better SNR than the 4-channel single-loop coil array.

Conclusion: Although B_1 fields are produced under the influence of the dielectric properties of the subject rather than the coil configuration alone at 7T, each RF coil exhibited not only special but also specific characteristics that could make it suited for specific application such as TMJ imaging.

Index words : Radiofrequency (RF) · Magnetic resonance imaging (MRI) · Ultrahigh-Field (UHF) · B_1 transmit · Temporomandibular joint (TMJ)

INTRODUCTION

Ultra-high field (UHF) magnetic resonance imaging (MRI) has the advantages of a higher signal-to-noise ratio (SNR) (1, 2) as well as enhanced susceptibility T_2* contrast (3, 4). However, it also has drawbacks, such as the inherent inhomogeneous radiofrequency (RF) magnetic (B_1) field as well as limited penetration depth. The later is often affected by wave interaction between subject and RF coil and could result in attenuation of RF penetration and asymmetric propagation of the electromagnetic (EM) wave inside the biological subject (5–7). For this reason, RF signal experiences distortion by the superposition of RF waves with different phases, especially at UHF MRI such as 7T (8).

In view of these intrinsic problems and in order to meet the specifications required for temporomandibular joint (TMJ) MR imaging at UHF, the optimal coil design is needed to provide an improved penetration depth as well as high SNR in the imaging region. Since all the obstacles to MR imaging at UHF such as 7T are closely related to the operating frequency of 300 MHz, selection of optimal coil configuration and their integration into the actual MR system appear to be the most critical factor (9). For the TMJ application, the most common coils used for TMJ imaging in high-field (HF) MRI were the single-channel circular-loop coil (10, 11) or a 4-channel receive (Rx)-only coil with

• Received; April 4, 2012 • Revised; August 13, 2012
• Accepted; August 16, 2012
Corresponding author : Zang-Hee Cho, Ph.D., Neuroscience Research Institute, Gachon University, 1198 Kuwol-dong, Namdong-gu, Incheon 405-760, Korea.
Tel. 82-32-460-2083, Fax. 82-32-460-8230, E-mail : zcho@gachon.ac.kr

externally separated transmit (Tx)-only coil (12). However, common approach to such as a single or multi-channel Rx-only surface coil in UHF appear to be limited by the absence of a local Tx capability. Moreover, the commercially available circularly polarized (CP) birdcage-based coil also appears to be limited by the relatively low B_1 strength in the peripheral region of the MR image due to the destructive wave interference at UHF (13, 14).

To improve the B_1 field efficiency in UHF, a number of methods have been proposed, including spiral birdcage coils (15, 16), use of adiabatic pulses (17), and parallel RF transmit (pTx), among others. Among the various approaches, one of the most promising approaches appears to be the RF excitation using a parallel transmits (18) and a multiple-element transmit array coil (19, 20). The later, appear to improve B_1 signal homogeneity, especially B_1^+ in the excited volume. The most important characteristics of the parallel RF excitations appear to be the improvement of the B_1 field and increased degrees of freedom of B_1^+ (21). The other promising method is modification of the RF coil configuration, which is changing the structure of the RF coil. Let us first look at the types of the RF coil currently available. Coil types can be categorized into two groups, namely the volume coil for entire volume imaging and surface coil for a dedicated and localized volume imaging, respectively. In the case of a localized volume imaging such as the TMJ region in human brain, a surface coil with high B_1 signal sensitivity usually preferred due to the high filling factor (FF) (22). Although the regions of B_1 sensitivity move away rapidly from the coil plane, yet the small surface coil provides high B_1 signal sensitivity at the near field region. To increase the FF more efficiently, namely to improve the B_1 signal sensitivity, the shape of the RF coil can be specifically optimized for the designated experiment. Since the surface coil allows direct access to the subject, variety of coil configurations (e.g., rectangular, circular, elliptical, polygonal windings etc) has been developed and verify of different performances in terms of B_1 sensitivity, penetration depth, and the RF power requirement have been observed.

Present study, therefore, focused on the RF coil design based on the computer modeling and simulation specifically directed to the 4-channel spiral-loop coil array for TMJ application at 7T. Computer simulation was performed for the single- and 4-channel loop coil array with different coil configurations (i.e., single-loop coil and spiral-loop coil). For these two types, results were evaluated in terms of penetration depth and B_1 signal distribution, including B_1^+ efficiency, using a cylindrical distilled water phantom and a human head model phantom, respectively. For the experiment at 7T, each of the 4-channel TMJ array coil was operated by home-built RF circuitry, such as a power divider (PD), Tx/Rx switching, and phase shifter (PS), specifically designed for TMJ imaging using a single RF amplifier source. The B_1 distribution and B_1^+ map of the water phantom were acquired using a 4-channel spiral-loop coil array and were compared with a 4-channel single-loop coil array. SNR maps of the human head were also measured and compared for each TMJ array coil in order to evaluate the B_1 field strength at 7T.

MATERIALS AND METHODS

System Hardware

The 7T whole-body MRI system (Magnetom 7T, Siemens Healthcare, Erlangen, Germany) is composed of a 900 mm bore superconducting magnet (Magnex Magnet Technology, Oxford, UK) connected to a Siemens Syngo console. A whole-body gradient coil is driven by Siemens gradient power amplifiers (GPA, 2000 V, 625 A) and has an inside diameter of 600 mm. System provides a maximum gradient strength of 40 mT/m in a minimum of 200 μs and slew rate of 200 T/m/s. For RF excitation and reception, a single source RF power amplifier (Dressler, Germany) and 32 channel receiver configuration were used.

Computer Modeling and Simulations

To obtain a desired B_1 strength at the desired location and overall field distribution, a commercially available EM simulation software tool, which equipped with a finite-difference time-domain method (XFDTD; REMCOM, State College, PA) for solving Maxwell's wave equations was used for computer simulation. The FDTD calculation was performed to reach −70 dB at the steady state. The post-processing of the result of the FDTD calculation was then carried out using MATLAB (The Mathworks, Matick, MA).

The single- and 4-channel loop coil array were

modeled before that used in the 7T imaging experiment. The phantom used for the EM simulation had a cylindrical shape with a diameter of 100 mm and a height of 50 mm. The dielectric properties assigned were 51.89 for electric permittivity (εr) and 0.55 for conductivity (σ, unit: S/m). These two values correspond to the mean value for the gray matter (εr = 60.02, σ = 0.69 S/m) and white matter (εr = 43.77, σ = 0.41 S/m) of the human brain at 300 MHz, respectively (23). Two different designs were modeled, one for the single-loop and the other for the spiral-loop Tx/Rx coil with 34 × 34 mm rectangular shape (Fig. 1a, b). The multi-turn spiral-loop planar coil (24–26) was designed with 4 turns of conductor traces each with width of 2 mm and 2 mm spacing between the conductor traces (Fig. 1b). The single-channel coil was then assembled and four coils are geometrically decoupled (Fig. 2). The overall dimensions of the assembled 4-channel coil array were 75 × 75 mm square with 4 mm distance between elements. The gapped coil arrangement (27) was chosen for its high decoupling efficiency with good B_1 profile as well as higher SNR distribution as compared with such as the overlapped design (28), shared conductor decoupling design (29), and decoupling by shielding design (30). In the final optimization, a capacitive decoupling (31) was added to more increase the decoupling efficiency (C_d in Fig. 2). The two kinds of 4-channel coil arrays, consisting of two coils in rows, was simulated with 180° out of phase condition (i.e., 0° for Ch.1 and Ch.3, 180° for Ch.2 and Ch.4 in Fig. 2) so as to focus the B_1^+ profile in the centerline along the main magnetic field direction (B_0, z-direction in Fig. 2) (32). For the more detailed comparison, the 4-channel spiral-loop coil array was simulated with loaded human head model and compared directly with the 4-channel single-loop coil array. First, the computer modeling of each single-channel coil was driven by 4

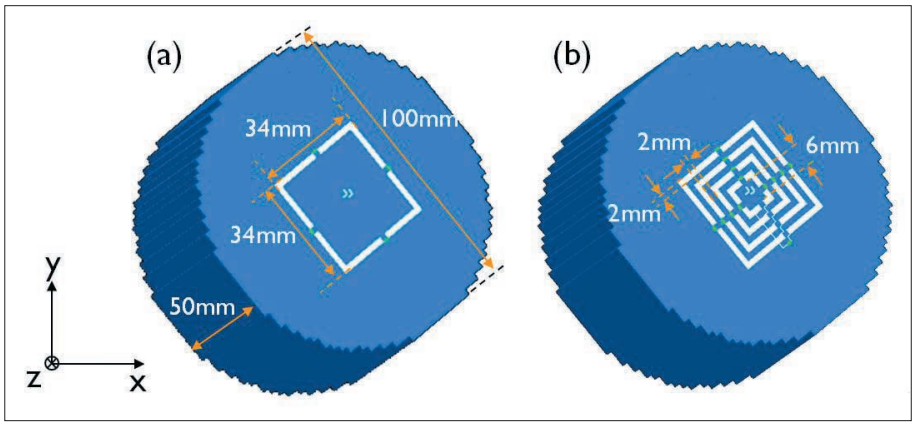

Fig. 1. Geometry of (a) single-channel single-loop coil and (b) single-channel spiral-loop coil, respectively. The spiral-loop coil was modeled with 4 turns of the coil with conductor trace width of 2 mm and trace spacing of 2 mm.

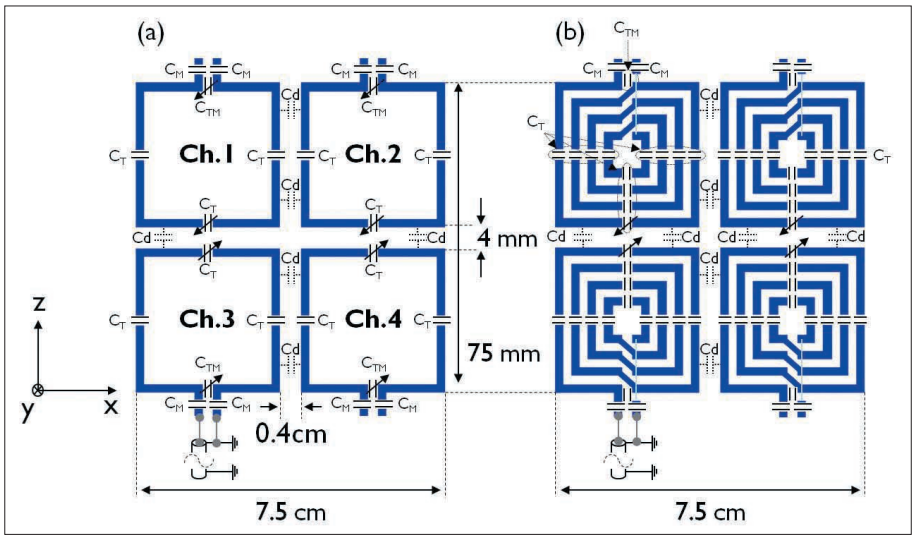

Fig. 2. Schematic representations of each 4-channel TMJ coil arrays with relevant dimensions. Coil layout for (a) 4-channel single-loop coil array and (b) 4-channel spiral-loop coil array, respectively Between the elements, 4 mm spacing was made. To eliminate mutual coupling between loops, a decoupling capacitors (C_d) was inserted between the loop coil elements.

and 13 current sources at the locations of the capacitors for the single-loop coil and spiral-loop coil, respectively. Thus, 16 and 52 current sources were used for each 4-channel coil array assembly. After the FDTD calculation, two rotating B_1 components (i.e., positive and negative CP component, B_1^+ and B_1^-) were extracted and recalculated for B_1 signal distribution (33),

$$B_1^+ = |(B_x + jB_y)/2|, \quad B_1^- = |(B_x + jB_y)^*/2| \qquad [1]$$

where the asterisk indicates the complex conjugate, and B_x and B_y denote the x and y components of B_1, respectively. The B_1 signal distribution was calculated under the assumption that T_1 and T_2 relaxation effects are negligible, as was the case of the B_0, i.e. (34),

$$\text{Signal Distribution} \propto W_c \sin(\gamma\tau V |B_1^+|)(|B_1^{-*}|) \qquad [2]$$

where W_c is water content, γ is the gyromagnetic ratio, τ is the pulse duration of transmit B_1 field, V is the coil driving voltage.

Construction of RF coil and Associate Circuitry

First, each single-channel TMJ coil was designed with FR4-based flexible circuit board and overlaid on the acrylic former. The conductor width and thickness of RF coils were chosen as 2 mm and 35 μm, respectively. A standard capacitive bridge circuit with matching capacitor (C_M) of 150 pF was used for impedance matching of 50 Ω. The single-channel single-loop coil was segmented into four sections in the coil loop with a fixed non-magnetic tuning capacitor (C_T, American Technical Ceramics, Series B non-magnetic) of 10 pF. One tuning and matching capacitor (C_{TM}) of 18 pF and 0.5–4 pF variable trimmer capacitor (NMKJ4HV, Voltronics Corporation) were used. While a fixed 15 pF capacitor for 13 sections was used in the single-channel spiral-loop coil. In case of two 4-channel loop coil arrays, the decoupling capacitor (C_d in Fig. 2) was used to reduce the crosstalk between adjacent elements.

The schematics of a total of 8 individual RF transmits for RF excitation of each 4-channel TMJ array coil by the existing single-channel RF amplifier were integrated with a 3-stage PD (Fig. 3). The designed PD is Wilkinson PD using lumped element components (Fig. 4). The two RF outputs are divided -3 dB power from RF input port and there is no phase shift between two RF output ports. It is connected with 100 Ω (2 $\times$ characteristic impedance (R) of 50 Ω). The inductance (L) and capacitance (C) are calculated by

$$L = R/(\sqrt{2}\pi f), \quad C = 1/(2\sqrt{2}\pi f R) \qquad [3]$$

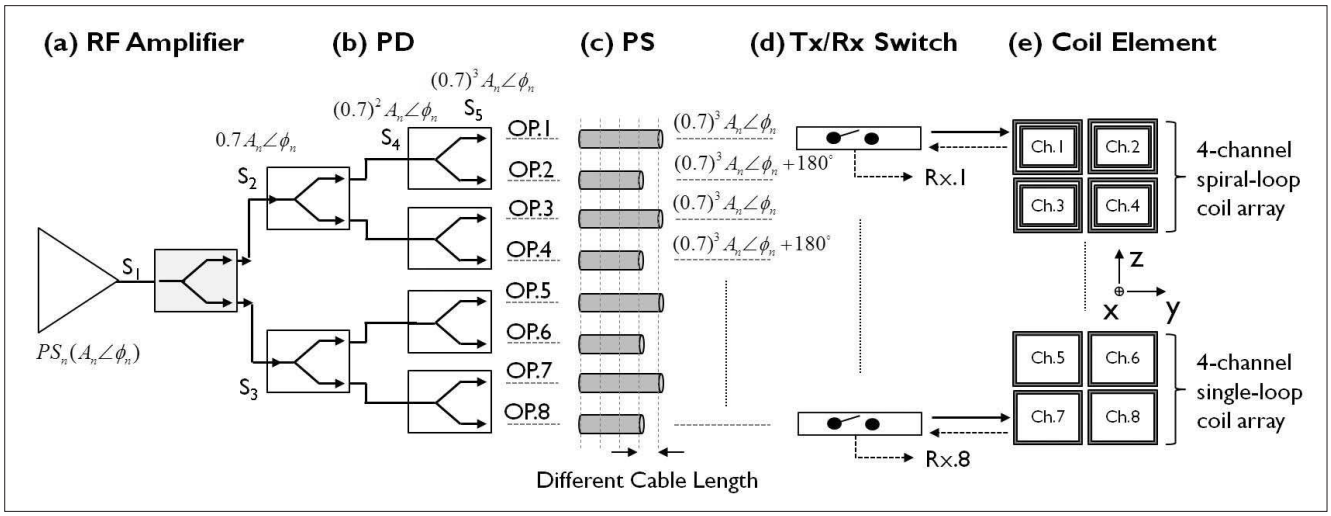

Fig. 3. RF signal pathway for two 4-channel TMJ coil arrays using the power divider (PD) and phase shifter (PS), and Tx/Rx switches. The RF signal comes from the (a) single-channel RF amplifier and is delivery to a (b) 2-way Wilkinson power dividers with -3dB power split and no phase shift. The final RF power signal is shifted via a (c) phase shifter using a coaxial cable delay. For the Tx/Rx operation, (d) Tx/Rx switches were inserted as a lumped element. The 8-output RF ports, two sets of coils with 4 each side, were connected to (e) each 4-channel TMJ coil arrays.

where f is operated center frequency of 297.2 MHz and L and C were calculated as 37.5 nH and 7.5 pF. The 3-stage PD was designed to provide fine matching between the single source of RF amplifier and 8-output RF transmit ports. The initial RF power signal from the amplifier (PS_n, Fig. 3a), with amplitude (A_n) and phase ($\emptyset$ n), is connected directly to the two Wilkinson PDs (Fig. 3b) in 1st stage and then divided again by the 3rd stage PD, thereby produced 8 RF power signals are produced. These RF signal were their fed to the PS (Fig. 3c) and then to the individual Tx/Rx switches (Fig. 3d). The final output signals are fed to the each coil element (Fig. 3e). The RF power signal from the RF amplifier was divided in 2-ways using a single Wilkinson PD at a resonance frequency of 297.2 MHz with −3 dB power (0.7 A_n) without phase shift ($\emptyset$ n). Each RF power signal from output port (indicated by OP.1 to OP.8 in the output stage of PD in Fig. 3b) was fixed at a constant amplitude ($\{0.7\}^3$ An) with a constant phase. The phase-shift (35) of each output RF power signal was adjusted by using different length of coaxial cable (RF 316 non-magnetic) (Fig. 3c). The cable length for 180° phase shift between the left and right side (i.e., Ch.1 and Ch.3 against to Ch.2 and Ch.4) of the loop coils in the arrays was measured with a vector network analyzer (NA) at 297.2MHz. Selected cable length of 180° phase shift was 36.2 cm. For Tx/Rx switching, a lumped element Tx/Rx switch was developed and utilized. It were controlled by the main part of PIN diode and insertion loss was minimized as well as the phase shift variance between the input (S_1 in Fig. 3b) and output ports (S_2, S_3 in Fig. 3b).

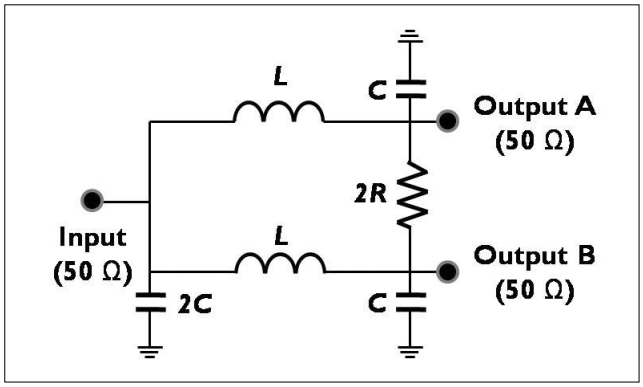

Fig. 4. Schematic circuit of the two-way Wilkinson power divider.

Data Acquisition Parameters

To evaluate the coil performance, MR imaging was performed using the distilled water phantom and studied B_1 field distribution as well as B_1^+ map. The imaging parameters used for the B_1 field measurement was the multi-slice two-dimensional gradient echo sequence (repetition time (TR) / echo time (TE) / FA (α) = 400 / 3.1 ms / 10°, 20°, 30°, 40°, and 60°, field-of-view (FOV) = 256 × 256 mm, matrix size = 256 × 256, slice thickness = 5 mm, number of slices = 10, and bandwidth = 260 Hz, total acquisition time = 1 min 42 s) and measurement was focused on to the central transverse orientation. For the investigation of B_1^+ map, the double angle method (DAM) was used (36). DAM technique requires two FAs, such as α and 2α with gradient recalled echo (GRE) imaging, identical to the imaging parameter for B_1 field distribution excepting 2α GRE imaging.

The human subject imaging was performed after the review by the human research committee. Subjects were examined in a supine position using two bilateral TMJ coil arrays on both sides of the human brain. Each 4-channel TMJ coil array assembly was positioned parallel to B_0 and the MR imaging was perform as a two-dimensional transverse image using magnetization-prepared rapid acquisition with gradient echo (MPRAGE) sequence (TR / TE / α = 8000 ms / 33 ms / 10°, FOV = 256 × 256 mm, matrix size = 512 × 512, slice thickness = 3.5 mm, number of slices = 1, and bandwidth = 470 Hz). Subsequently, TMJ region imaging of the human brain was performed in sagittal orientation. The imaging parameters chosen were a T_1 weighted three-dimensional fast low angle shot (FLASH) sequence (TR / TE / α = 16 / 3.42 ms / 10°, FOV = 200 × 200 mm, matrix size = 320 × 320, slice thickness = 0.6 mm, bandwidth = 200 Hz, and total acquisition time = 6 min 10 s).

RESULTS

Computer Modeling and Simulations

First, each single-channel Tx/Rx coils, namely single-loop coil and spiral-loop coil, were compared in terms of B_1 field (Fig. 5a, b) and B_1^+ map (Fig. 5c, d) as well as B_1^+ profile (Fig. 5e) at 300 MHz. The simple calculation for the SNR map, ignoring the relaxation effects

(i.e., T_1 and T_2) as well as the B_0 effect was performed. All the field distributions were then compared after normalization with the dimensionless normalization factor V (which was necessary to create a normalized field magnitude, VB_1^+ which is equal to 3 μT) (37). This corresponds to producing an FA of 90° in hydrogen (^{1}H) with a 2-ms rectangular RF pulse (38) at a distance of 20 mm (Fig. 5c) away from the coil plane.

According to measurement, the B_1 field of the single-channel spiral-loop coil (Fig. 5b) was substantially stronger than the single-loop coil (Fig. 5a) at the near the coil plane. The B_1^+ distribution in the phantom (dotted line of box in Fig. 5a, b) was compared for the two single-channel Tx/Rx coils. As shown in Fig. 5e, the B_1^+ of the spiral-loop coil is substantially stronger at the near field region which corresponds to the coil plane. B_1^+ of the spiral-loop coil was nearly three times larger than that of the single-loop coil (i.e., 5.11e–0.05 and 1.73e–0.05 for spiral-loop coil and single-loop coil in the FDTD calculation).

A direct comparison of the B_1 field and B_1^+ distribution of two coils, i.e., single-loop coil and spiral-loop coil (Fig. 6a, b) was also performed in the human head model for each 4-channel TMJ coil array assembly. The distance between boundary of excitation profile inside of the human head and the TMJ array coil was ranged from minimum 6 mm to maximum 16 mm. The 4-channel spiral-loop coil array showed again consistently higher excitation profile (Fig. 6e) and high B_1 signal intensity (Fig. 6c) compared to the 4-channel single-loop coil array. Notable results of the simulation is that the B_1 signal intensity of the 4-channel spiral-loop coil in the region of interest corresponding to the end of the human head was nearly twice larger than the 4-channel single-loop coil (5.8e–008 and 2.5e–008 for spiral and rectangular geometry in the FDTD calculation) suggesting that the 4-channel spiral-loop coil array is the choice for the TMJ imaging.

Experimental Results of the Two 4-channel TMJ Coil Arrays

According to the computer simulation results, a 4-channel spiral-loop coil array and a 4-channel single-

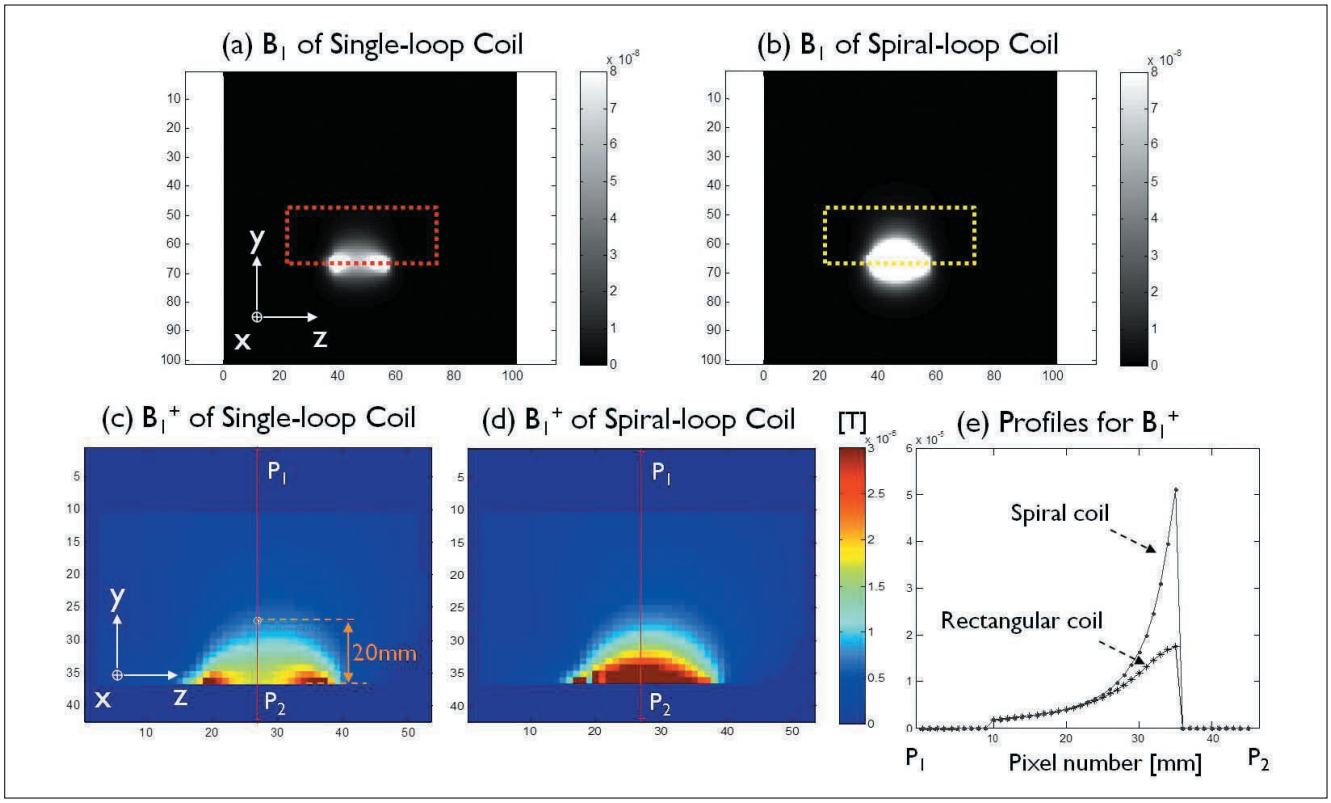

Fig. 5. Computer simulation of relative (a, b) B_1 field distribution and (c, d) B_1^+ maps for single-channel single-loop and spiral-loop coil was acquired by FDTD calculation. The B_1^+ maps of each coil were compared after normalization with 3 μT in a location 20 mm apart from the coil plane. The color scale is expressed in terms of a fraction of the maximum scale value. (e) The B_1^+ profiles on the line of P_1 and P_2 (in Fig. 5c, d).

loop coil array were constructed and attached directly onto the water phantom (Fig. 7a, b for 4-channel spiral-loop and single-loop coil array, respectively). Tuning, matching, and capacitive decoupling for the coil array was thoroughly examined at 297.2 MHz and matched to 50 Ω. For the experiment, the distilled water phantom (Composition: 1.25 g$NiSO_4$ × 6H_2O +5 g$NaCl$ per 1000 H_2O; size of 20 cm × 20 cm × 30 cm, in the x, y, and z directions, respectively) was used.

The reflection coefficient (S_{11}) and transmission loss (S_{12}, S_{13}, and S_{14}) of the two 4-channel TMJ coil arrays

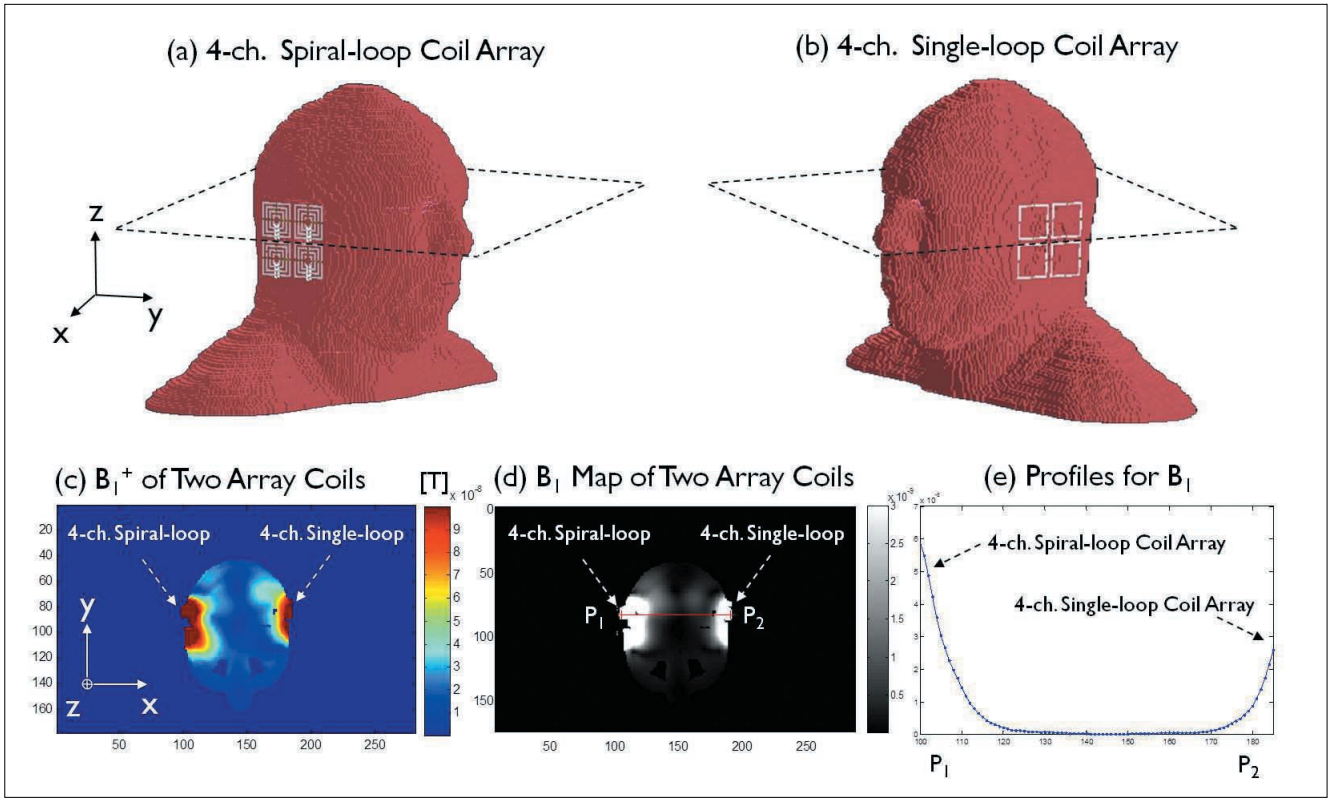

Fig. 6. Computer simulation results of (a) the 4-channel spiral-loop coil array and (b) 4-channel single-loop coil array, respectively in a human head model. (c) The B_1^+ maps and (d) B_1 field in the central transverse plane (dotted line in (a, b)) at 300 MHz. (e) The B_1 profile shown with blue line (P_1–P_2 line in (d)) indicates the corresponding SNR map.

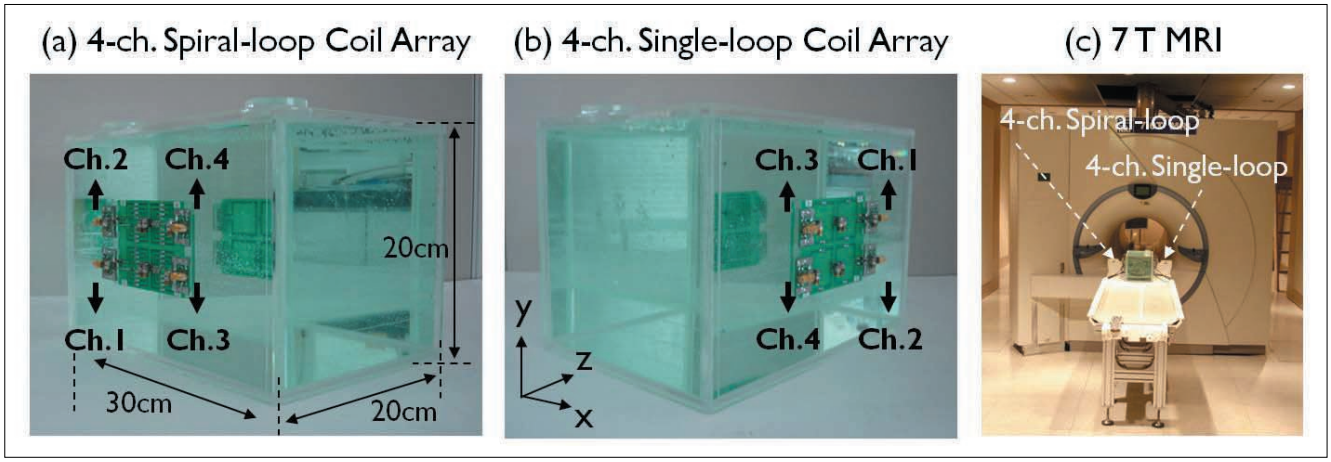

Fig. 7. Two types of 4-channel TMJ coil arrays; (a) the spiral-loop coil array and (b) the single-loop coil array. For the experimental setting, both coils are attached onto the distilled water phantom (composition: 1.25 g$NiSO_4$ × 6H_2O + 5 g$NaCl$ per 1000 H_2O, size 20 cm × 20 cm × 30 cm in the x, y, and z directions). (c) is the experimental setting at 7T MRI.

were measured and found to be better than −20 dB and −6 dB, respectively for each element. To further decrease the mutual inductance coupling (S_{12}, S_{13}, and S_{14}) between the neighboring elements, capacitive decoupling techniques (31) was adopted in a slightly different position (C_d in Fig. 2) for two 4-channel TMJ coil arrays and reduced crosstalk was to a maximum of −10.4 dB for the 4-channel single-loop coil array and −14 dB for the 4-channel spiral-loop coil array, respectively while maintaining an input match (S_{11}) of better than −25 dB on all coils. The observed reflection coefficient and transmission loss using a decoupling capacitor of 10 pF-20 pF were measured at a center frequency of 297.2 MHz (Table 1). The quality-factor (Q-factor) ratio was calculated from unloaded Q (Q_U) divided by loaded Q-factor (Q_L) and measured with a vector NA. The mean value of Q-factor ratio for four spiral-loop coil is 5.4 (159.3 for Q_U and 29.2 for Q_L). The RF circuit, including the Tx/Rx switches, PD, and PS, were carefully optimized and measured using vector NA. The observed transmission loss, including the power loss and phase shifts of Wilkinson PD between the input and output ports, was approximately −3.35 dB with no phase difference (S_{21} in Fig. 3b). The phase difference of the two output ports between S_{21} and S_{31} (in Fig. 3b) was

Table 1. S-parameter Measurements Obtained Under Two Conditions: a Coil Loaded with Phantom (without parenthesis) and Additional Capacitive Decoupling (values within the parenthesis). The Values are Given in dB.

(a) 4-ch. Rectangular Array Coil

	S1	S2	S3	S4
S1	-21.7 (-33.9)	-7.10 (-15.1)	-11.06 (-13.8)	-6.01 (-17.5)
S2		-24.1 (-29.6)	-6.15 (-16.9)	-10.9 (-14.4)
S3			-29.9 (-37.7)	-7.24 (-16.4)
S4				-33.3 (-29.3)

(b) 4-ch. Spiral Array coil

	S1	S2	S3	S4
S1	-29.7 (-28.4)	-9.1 (-13.2)	-9.4 (-10.5)	-8.6 (-19.9)
S2		-22.5 (-27.1)	-8.4 (-22.4)	-18.1 (-12.5)
S3			-25.7 (-34.1)	-8.6 (-10.4)
S4				-25.1 (-26.8)

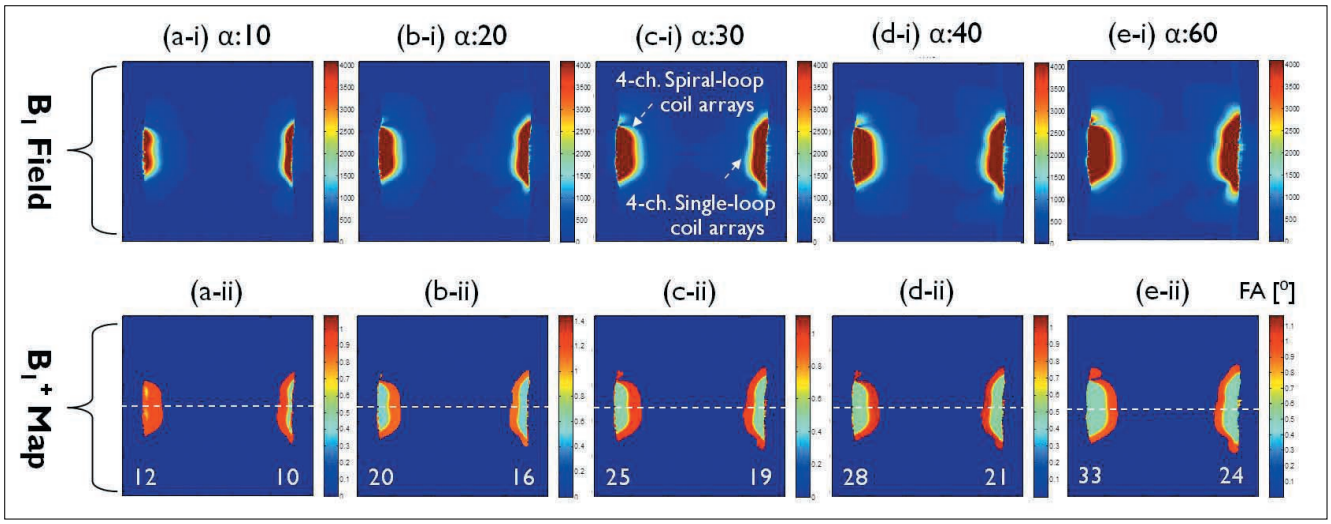

Fig. 8. Upper part; B_1 field distributions in phantom obtained by GRE imaging for each 4-channel TMJ coil arrays for different FA values; 10°, 20°, 30°, 40°, and 60°. Lower part; B_1^+ maps obtained for different values of FA. FA was normalized for the central transverse plane at 7T.

found to be less than $\pm 1^{\circ}$. In addition, the isolation and directivity were found to be satisfactory, approximately −30 dB at 297.2 MHz. Performance of each Tx/Rx switching was measured and found to be approximately −22 dB for return loss with only small phase difference ($\geq 0.5^{\circ}$) between each transmission path. The phase difference of 180° was achieved by an extra cable length of 36.2 cm (-53.46°) together with the reference RG 316 cable which shifted the phase is 126.22°.

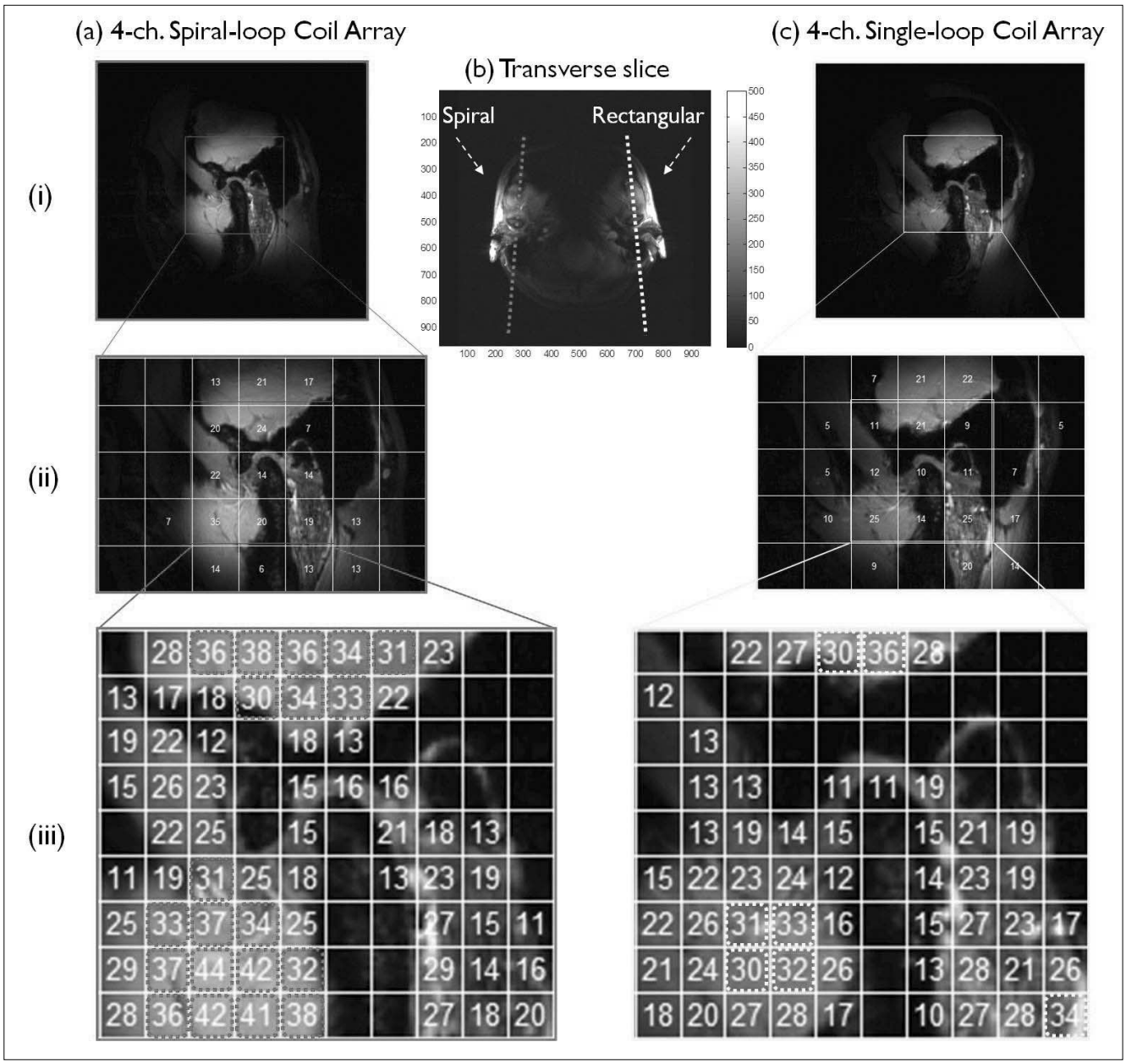

Fig. 9. MRI images obtained from the TMJ region using 3D FLASH sequence (TR / TE / α = 16 / 3.42 ms / 10°, field-of-view = 200 × 200 mm, matrix size = 320 × 320, slice thickness = 0.6 mm, bandwidth = 200 Hz, and total acquisition time = 6 min 10 s). SNR maps in the TMJ image were obtained from both (a-i) 4-channel spiral-loop coil array (c-i) 4-channel single-loop coil array, respectively, while in the middle (b-i), a corresponding transverse slice are shown. In the bottom row (iii), SNR maps of the 4-channel spiral-loop coil array and the 4-channel single-loop coil array are shown. The numerical values shown are the SNR values. As shown 4-channel spiral-loop coil array has better image intensity profile than the single-loop coil for specific SNR value (dotted line of box indicate SNR of 30 and over).

Experimental Results of Phantom and Human Studies

To confirm the computer simulation results, the B_1 field and B_1^+ maps were experimentally measured and compared with 7T MRI. The central transverse B_1 field was measured for several different FA values (i.e., α = 10°, 20°, 30°, 40°, and 60°) values and the results are shown (in upper row of Fig. 8). The transverse images illustrate the changes in MR image intensity in the water phantom with increasing excitation power, i.e., FA values (25). The data indicate that the excitation RF profile corresponding to increasing changes in FA value could produce sufficient imaging depth and demonstrated that the coil can be useful for the TMJ imaging. Note that the 4-channel spiral-loop coil array had a smaller imaging region or B_1 field, but, the imaging depth was deeper than the 4-channel single-loop coil array.

The two-dimensional B_1^+ maps for a given FA (2 α) in the distilled water phantom were calculated using DAM (in lower row of Fig. 8). This B_1^+ map was normalized for a given FA value (bottom row of Fig. 8). The B_1^+ map of the 4-channel spiral-loop coil array produced a distribution that had a higher FA inside the subject and was more focused around the central region. For quantitative comparison of the B_1^+ map, each B_1^+ map was filtered with masking using a constant value of 0.6 for the maximum value of it. The 1D profile was measured in the central region (dotted line in lower row of Fig. 8) and the number of pixels was counted. The total number of pixels was converted to a distance expressed by a number (bottom corners in lower row of Fig. 8). The results indicate that the relative distance for B_1^+ profile of 4-channel spiral-loop coil array for different FA was substantially higher than the 4-channel single-loop coil array (i.e., distance = 12, 20, 25, 28, and 33 for different FA in the 4-channel spiral-loop coil array while 10, 16, 19, 21, and 24 for single-loop coil array).

For human TMJ imaging, the B_1 field distribution was measured in sagittal slices (Fig. 9a, c) and then SNR map was compared. The TMJ image was obtained in a slightly oblique sagittal orientation perpendicular to the long axis of the condylar head (12). The SNR measurements were based on the National Electrical Manufactures Association (NEMA) method (39) and were obtained by dividing the average signal intensity inside the human image by the standard deviation (SD) of the noise in the specific region (ROI, 10 × 10 pixel) which is placed in the outside the imaging region. The mean SNR was measured for large and small areas (in the middle and lower rows of Fig. 9). The calculated mean SNR of the TMJ MR image from the 4-channel spiral-loop coil array showed marginal superiority to that of the 4-channel single-loop coil array.

DISCUSSION AND CONCLUSION

In this study, the 4-channel spiral-loop coil array against the general geometry of 4-channel single-loop coil array for TMJ imaging was evaluated. RF circuitry suitable for the coils as well as two set of array coils were designed and experimentally compared for B_1 field distribution as well as SNR at 7T using a water phantom and human. Evaluation parameters specifically chosen are B_1, B_1^+, and SNR. In the computer simulation, B_1^+ field of the designed 4-channel spiral-loop coil array were substantially superior compared to the single-loop coil arrays. Moreover, 4-channel spiral-loop coil array also showed superior strength in B_1^+ map and higher depth profile in the human brain model than 4-channel single-loop coil array. That is, the spiral-loop coil has a higher B_1 excitation profile with sufficient imaging depth in the TMJ region in human brain model.

The experimental results, however, the mean SNR value in the human TMJ image was slightly higher for the 4-channel spiral-loop coil array than for the 4-channel single-loop coil array (Fig. 9). Because present study assumed that the RF coil, circuitry such as Tx/Rx switches, PD, PS, preamplifier performance, and so on, were perfect, the performance of the RF coil and RF circuitry for this study relied on only the S-parameter as a bench test. In other words, the B_1 signal distribution of the TMJ image was determined from only the signal, without the noise term. The noise level is an important factor in the evaluation of the performance of an array coil. To confirm its performance for no observable change in signal variance, it can be clearly compared using a noise correlation matrix (NCM) or geometry factor (g-factor). Therefore, in a further study, the RF coil and circuitry will have to be considered more carefully in order to achieve optimal noise conditions.

Previous work has shown the feasibility of multi turns spiral windings by computational simulation process using Biot-Savart equation and flat spiral coil with 4 turns yielded the best maximum B_1 field intensity and its penetration depth (26). Although planar spiral surface coil allows direct access to the sample to increase coil's B_1 field strength, but with decreasing the B_1 field uniformity. Therefore, the structure (i.e., spacing of tracer and copper width) of the spiral geometry has to be considered closely for improving its in-plane B_1 field homogeneity (24).

Another consideration is that how to eliminate the interactions such as mutual inductance coupling between surface coils. Mutual inductance coupling causes splitting of the resonance frequency and thus decreased image sensitivity and increased power loss in RF coil can be occurred. Although gapped coil geometry and additional capacitively decoupled approach was implemented in this study, several technical methods (e.g., geometrically overlapped surface coil for adjacent coil, shared coil conductor decoupling, gapped coil, or decoupling by external shielding) could be considered in future study.

The results both computer simulation and corresponding experimental study indicated that dedicated 4-channel spiral-loop coil array appears to provides high quality images with a better imaging depth at 7T compared with single-loop coil. It is, therefore, appears sufficient to apply in TMJ imaging, including intra-articular disc and bone structures etc, among others (40, 41). Although the experimental results are not as superior as expected from the computer simulation, the finding of the greater penetration depth and marginally improved sensitivity compared to the 4-channel single-loop coil array is promising. Serendipity of present study is that the modifications could be extended to the other applications such as inner ears, internal auditory canal, and orbits.

Acknowledgements:

This work was supported by the National Research Foundation (NRF), the Ministry of Education, Science and Technology (2008-2004159) and supports from the Gil foundation.

References

1. Hoult DI, Richards RE. The signal to noise ratio of the nuclear magnetic resonance experiment. J Magn Reson 1976;24:71-85
2. Wiesinger F, Van de Moortele PF, Adriany G, Zanche ND, Ugurbil K, Pruessmann KP. Potential and feasibility of parallel MRI at high field. NMR Biomed 2006;19:368-378
3. Abduljalil AM, Robitaille P-ML. Macroscopic susceptibility in ultra high field MRI. J Comput Assist Tomogr 1999;23:832-841
4. Abduljalil AM, Kangarlu A, Yu Y, Robitaile P-ML. Macroscopic susceptibility in ultra high field MRI. II: acquisition of spin echo images from the human head. J Comput Assist Tomogr 1999;23:842-844
5. Bottomley PA, Andrew ER. RF magnetic field penetration, phase shift and power dissipation in biological tissue: implications for NMR imaging. Phys Med Biol 1978;23:630-643
6. Roschmann P. Radiofrequency penetration and absorption in the human-body: limitations to high-field whole-body nuclear magnetic resonance imaging. Med Phys 1987;14:922-931
7. Bomsdorf H, Helzel T, Kunz D, Roschmann P, Tschendel O, Wieland J. Spectroscopy and imaging with a 4 tesla whole-body mr system. NMR Biomed 1988;1:151-158
8. Cho ZH, Kim YB, Kim KN, Hong SM. MRI system RF coil assembly with a birdcage transmit only coil and a pseudo-chain-link receive only coil array. 2010; US 7,733,088 B2
9. Wald LL, Wiggins GC, Potthast A, Wiggins CJ, Triantafyllou C. Design consideration and coil comparisons for 7T brain imaging. Appl Magn Reson 2005;29:19-37
10. Eberhard D, Bantleon HP, Steger W. Functional magnetic resonance imaging of temporomandibular joint disorders. Eur J Orthod 2000;22:489-497
11. Welker KN, Tsuruda JS, Hadley JR, Hayes CE. Radio-frequency coil selection for MR imaging of the brain and skull base. Radiology 2001;221:11-25
12. Zhang S, Gersdorff N, Frahm J. Real-time magnetic resonance imaging of temporomandibular joint dynamics. The Open Medical Imaging Journal 2011;5:1-7
13. Vaughan JT, Garwood M, Collins CM, et al. 7T vs. 4T: RF power, homogeneity, and signal-to-noise comparison in head images. Magn Reson Med 2001;46:24-30
14. Van de Moortele PF, Akgun C, Adriany G, et al. B1 destructive interference and spatial phase patterns at 7T with a head transceiver array coil. Magn Reson Med 2005;54:1503-1518
15. Alsop DC, Connick TJ, Mizsei G. A spiral volume coil for improved RF field homogeneity at high static magnetic field strength. Magn Reson Med 1998;40:49-54
16. Mueller MF, Blaimer M, Breuer F, et al. Double spiral array coil design for enhanced 3D parallel MRI at 1.5 Tesla. Concept in Magn Reson Part B 2009;35:67-79
17. Staewen RS, Johnson AJ, Ross BD, Parrish T, Merkle H, Garwood M. 3D flash imaging using a single surface coil and a new adiabatic pulse, BIR-4. Invest Radiol 1990;25:559-567
18. Katscher U, Borner P, Leussler C, Van de Brink JS. Transmit SENSE. Magn Reson Med 2003;49:144-150
19. Adriany G, Van de Moortele PF, Ritter J, et al. A geometrically adjustable 16-channel transmit/receive transmission line array for improved RF efficiency and parallel imaging performance at 7Tesla. Magn Reson Med 2008;59:590-597
20. Kim KN, Darji N, Herrmann T, et al. Improved B1+ field using 16-channel transmit head array and an 8-channel pTx system at 7T. In: Proceedings of the 20th Annual Meeting of ISMRM, Montreal, 2011, p 3220
21. Clare S, Alecci M, Jezzard P. Compensating for B1 inhomogeneity using active transmit power modulation. Magn Reson

Imaging 2001;19:1349-1352
22. Mispelter J, Lupu M, Briguet A. NMR probeheads for biophysical and biomedical experiments: theoretical principles & practical guidelines. Imperial College London 2006
23. Gabriel C. Internet document; URL: http://niremf.ifac.cnr.it/tissprop/#over
24. Eroglu S, Gimi B, Roman B, Friedman G, Magin RL. NMR spiral surface microcoils: design, fabrication, and imaging. Concepts in Magn Reson Part B 2003;17:1-10
25. Gimi B, Eroglu S, Leoni L, Desai TA, Magin RL, Roman BB. NMR spiral surface microcoils: applications. Concepts in Magn Reson Part B 2003;18:1-8
26. Constantinides C, Angeli S, Gkagkarellis S, Cofer G. Intercomparison of performance of RF coil geometries for high field mouse cardiac MRI. Concepts in Magn Reson Part A 2011;38:236-252
27. De Zwart JA, Ledden PJ, Kellman P, van Gelderen P, Duyn JH. Design of a SENSE-optimized high-sensitivity MRI receive coil for brain imaging. Magn Reson Med 2002;47:1218-1227
28. Roemer PB, Edelstein WA, Hayes CE, Souza SP, Mueller OM. The NMR phased array. Magn Reson Med 1990;16:192-225
29. Wang J. A novel method to reduce the signal coupling of surface coils for MRI. In: Proceedings of the 4th Annual Meeting of ISMRM, 1996, p 1434
30. Deppe MH, Parra-Robles J, Marshall H, Lanz T, Wild JM. A flexible 32-channel receive array combined with a homogeneous transmit coil for human lung imaging with hyperpolarized 3He at 1.5T. Magn Reson Med 2011;66:1788-1797
31. Morze CV, Tropp J, Banerjee S, et al. An eight-channel, nonoverlapping phased array coil with capacitive decoupling for parallel MRI at 3T. Concepts in Magn Reson Part B 2007;31:37-43
32. Kraff O, Bitz AK, Kruszona S, et al. An eight-channel phased array RF coil for spine MR imaging at 7T. Invest Radiol 2009;44:734-740
33. Yang QX, Wang J, Zhang X, et al. Analysis of wave behavior in lossy dielectric samples at high field. Magn Reson Med 2002;47:982-989
34. Collins CM, Yang QX, Wang JH, et al. Different excitation and reception distribution with a single-loop transmit-receive surface coil near a head-sized spherical phantom at 300 MHz. Magn Reson Med 2002;47:1026-1028
35. Dole CW. Coaxial cable insertion phase measurement and analysis. Internet document; URL: http://www.belden.com/pdfs/Techpprs/Wireless%20Market%20Web%20Phase%20Paper.pdf, Accessed March 10, 2012
36. Cunningham CH, Pauly JM, Nayak KS. Saturated double-angle method for rapid B1+ mapping. Magn Reson Med 2006;55:1326-1333
37. Collins CM, Smith MB. Calculation of B1 distribution, SNR, and SAR for a surface coil adjacent to an anatomically-accurate human body model. Magn Reson Med 2001;45:692-699
38. Collins CM, Smith MB. Signal-to-noise ratio absorbed power as functions of main magnetic field strength, and definition of "90°" RF pulse for the head in the birdcage coil. Magn Reson Med 2001;45:684-691
39. NEMA standards publication MS-2001
40. Dalkiz M, Pakdemirli E, Beydemir B. Evaluation of temporomandibular joint dysfunction by magnetic resonance imaging. Turk K Med Sci 2001;31:337-343
41. Maizlin ZV, Nutiu N, Dent PB, et al. Displacement of the temporomandibular joint disk: correlation between clinical findings and MRI characteristics. J Can Dent Assoc 2010;76:a3

대한자기공명의과학회지 16:103-114(2012)

7T 악관절 MRI를 위한 4 채널 스파이럴 RF 코일의 성능개선

가천대학교 뇌과학연구소

김경남 · 김영보 · 조장희

목적: 7T 악관절 자기공명상의 개선을 위해 제안된 4 채널 스파이럴 코일과 그를 구동시키기 위한 회로는 자기장의 분포, 송신 전용필드, 신호 대 잡음 비, 그리고 악관절 영상에 대하여 일반적인 단일 루프 형태의 코일과 비교되었다.
대상과 방법: 단일 채널 그리고 4 채널 스파이럴 코일은 단일 루프 형태의 코일에 대해 전자기장 시뮬레이션으로 자기장의 분포 및 송신 전용 필드에 대해서 비교 되었고, 7T에서 이를 평가하고자 송신전용 필드와 더불어 자기장의 분포 역시 비교 평가되었다.
결과: 전자기장 시뮬레이션의 결과와 7T 자기공명영상에서 4 채널 스파이럴 코일은 기존에 사용되는 일반적인 구조인 단일 루프 코일에 비해 상대적으로 우수한 자기장의 분포 및 송신 전용 필드를 보였다.
결론: 7T에서는 코일의 구조에 비해 상대적으로 영상화되는 물질의 특성에 더욱더 의존적이나, 각각의 코일은 다른 필드 분포를 나타냄으로써 최적화된 코일은 악관절 영상과 같은 특정 용도로 사용될 수 있음을 확인하였다.

통신저자 : 조장희, (405-760) 인천광역시 남동구 구월 1동 1198번지, 가천대학교 뇌과학연구소
Tel. (032) 460-2083 Fax. (032) 460-8230 E-mail: zcho@gachon.ac.kr